

**Title: Potassium dependent structural changes in the selectivity filter of HERG potassium channels**

**Authors:** Carus H.Y. Lau<sup>1,2†</sup>, Emelie Flood<sup>3†</sup>, Mark J. Hunter<sup>1,2†</sup>, Billy J Williams-Noonan<sup>3</sup>, Karen M. Corbett<sup>3</sup>, Chai-Ann Ng<sup>1,2</sup>, James C. Boucher<sup>4</sup>, Alastair G. Stewart<sup>2,5</sup>, Eduardo Perozo<sup>6</sup>, Toby W. Allen<sup>3\*</sup>, Jamie I. Vandenberg<sup>1,2\*</sup>

**Supplementary Material**

Table S1: Cryo-EM data collection, refinement, and validation statistics

Table S2: Key resources table

Figure S1: Cryo-EM data processing workflow

Figure S2: Cryo-EM validation statistics

Figure S3: TMD densities for high-K and low-K

Figure S4: Ramachandran plots for high-K and low-K pdb

Figure S5: MDFF fits to cryo-EM maps for high and low-K structures.

Figure S6: Hole profiles of HERG high- and low-K compared to KcsA.

Figure S7: Ion conduction events in HERG

Figure S8: Constrained ion MD simulations to explore the effect of K<sup>+</sup> ions on selectivity filter conformation.

Figure S9: REST2 simulations of HERG

Figure S10: Cluster analysis of constrained ion MD simulations

Figure S11: Interactions behind the selectivity filter for MD simulations with different K<sup>+</sup> ion conformations.

Figure S12: Changes in water distribution behind the selectivity filter

Figure S13: 2-dimensional free energy maps for V625 carbonyl oxygen flipping

Movie S1: Transition between conducting and non-conducting states

Supplementary References

**Supplementary Table S1. Cryo-EM data collection, refinement and validation statistics**

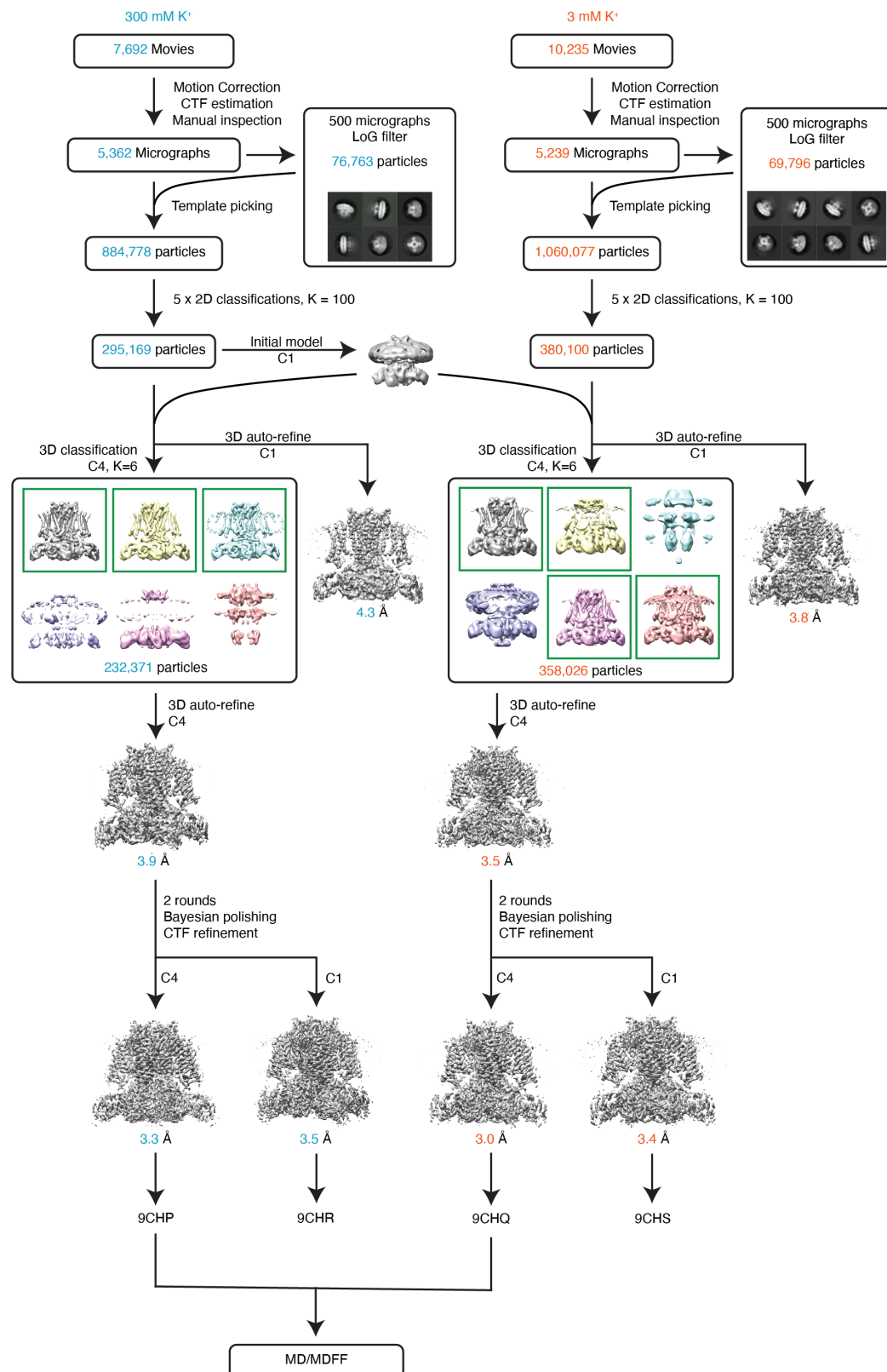
	300 mM K <sup>+</sup> C4 symmetry (EMDB-45597) (PDB 9CHP)	300 mM K <sup>+</sup> C1 symmetry (EMDB-45599) (PDB 9CHR)	3 mM K <sup>+</sup> C4 symmetry (EMDB-45598) (PDB 9CHQ)	3 mM K <sup>+</sup> C1 symmetry (EMDB-45600) (PDB 9CHS)
<b>Data collection and processing</b>				
Magnification	130,000 x		130,000 x	
Voltage (kV)	300		300	
Electron exposure (e <sup>-</sup> /Å <sup>2</sup> )	50		50	
Defocus range (μm)	-0.6 to -2.5		-0.6 to -2.5	
Pixel size (Å)	1.05		1.05	
Symmetry imposed	C4	C1	C4	C1
Initial particle images (no.)	884,778		1,060,077	
Final particle images (no.)	232,371		358,026	
Map resolution (Å)	3.3	3.5	3.0	3.4
FSC threshold	0.143	0.143	0.143	0.143
Map resolution range (Å)	3.2 – 5.4	3.4 – 5.9	2.9 – 4.9	3.3 – 5.5
<b>Refinement</b>				
Initial model used	5VA1	This study	5VA1	This study
Model resolution (Å)	3.4	3.6	3.1	3.4
FSC threshold	0.5	0.5	0.5	0.5
Model resolution range (Å)				
Map sharpening <i>B</i> factor (Å <sup>2</sup> )	-103.7	-84.1	-88.5	-91.5
Model composition				
Non-hydrogen atoms	9508		9508	
Protein residues	1172		1172	
Ligands	0		0	
<i>B</i> factors (Å <sup>2</sup> )				
Protein	51.51	61.87	63.45	55.63
Ligand	n.a.	n.a.	n.a.	n.a.
R.m.s. deviations				
Bond lengths (Å)	0.013	0.012	0.013	0.012
Bond angles (°)	1.747	1.867	1.730	1.862
Validation				
MolProbity score	0.5	0.5	0.5	0.53
Clashscore	0.00	0.00	0.00	0.00
Poor rotamers (%)	0.00	0.00	0.00	0.00
Q-score	0.496	0.477	0.527	0.498
Ramachandran plot				
Favored (%)	98.25	98.07	98.6	97.89
Allowed (%)	1.75	1.93	1.4	2.11
Disallowed (%)	0.0	0.0	0.0	0.0

**Supplementary Table S2. Key resources table**

REAGENT or RESOURCE	SOURCE	IDENTIFIER
<b>Bacterial and virus strains</b>		
<i>E. coli</i> DH5- $\alpha$	New England Biolabs	Cat# C2987H
<i>E. coli</i> DH10Bac	Thermo Fisher Scientific	Cat# 10361-012
<b>Chemicals, peptides, and recombinant proteins</b>		
FreeStyle™ 293 Expression Medium	GIBCO	Cat# 12338026
Sf-900™ III SFM	GIBCO	Cat# 12658019
n-Dodecyl-b-D-Maltoside (DDM)	Anatrace	Cat# D310
Cholesteryl hemisuccinate	Anatrace	Cat# CH210
1-palmitoyl-2-oleoyl-sn-glycero-3-phosphocholine (POPC)	Avanti Polar Lipids	Cat# 850457
1-palmitoyl-2-oleoyl-sn-glycero-3-phosphoethanolamine (POPE)	Avanti Polar Lipids	Cat# 850757
1-palmitoyl-2-oleoyl-sn-glycero-3-phosphate (POPA)	Avanti Polar Lipids	Cat# 840857
<b>Deposited data</b>		
HERG WT high-K atomic model and density map	This study	PDB: 9CHP; EMDB: 45597
HERG WT low-K atomic model and density map	This study	PDB: 9CHQ; EMDB: 45598
HERG WT high-K atomic model and density map without symmetry	This study	PDB: 9CHR; EMDB: 45599
HERG WT low-K atomic model and density map without symmetry	This study	PDB: 9CHS; EMDB: 45600
<b>Experimental models: Cell lines</b>		
Spodoptera frugiperda (Sf9)	GIBCO	Cat# 12659017
HEK293S GnTI <sup>-</sup>	ATCC	Cat# CRL-3022
Stable HERG expressing HEK293	Ng et al. <sup>1</sup>	N/A
<b>Experimental models: Organisms/strains</b>		
<i>Xenopus laevis</i>	Nasco	N/A
<b>Recombinant DNA</b>		
HERG WT	This study	N/A
HERG N588E	This study	N/A
HERG N588K	This study	N/A
<b>Software and algorithms</b>		
RELION 3.1.1	Zivanov et al. <sup>2</sup>	<a href="https://www3.mrc-lmb.cam.ac.uk/relion/">https://www3.mrc-lmb.cam.ac.uk/relion/</a>
ChimeraX 1.3	Pettersen et al. <sup>3</sup>	<a href="https://www.cgl.ucsf.edu/chimerax/">https://www.cgl.ucsf.edu/chimerax/</a>
ISOLDE 1.3	Croll <sup>4</sup>	<a href="https://isolde.cimr.cam.ac.uk/">https://isolde.cimr.cam.ac.uk/</a>
CTFFIND 4.1.14	Rohou et al. <sup>5</sup>	<a href="https://grigoriefflab.umassmed.edu/ctffind4">https://grigoriefflab.umassmed.edu/ctffind4</a>
EPU	Thermo Fisher Scientific	N/A
PHENIX 1.20.1-4487	Liebschner et al. <sup>6</sup>	<a href="https://phenix-online.org/">https://phenix-online.org/</a>

HOLE	Smart et al. <sup>7</sup>	<a href="http://www.holeprogram.org/">http://www.holeprogram.org/</a>
MolProbity	Chen et al. <sup>8</sup>	<a href="http://molprobity.biochem.duke.edu/">http://molprobity.biochem.duke.edu/</a>
TEMPy:Diffmap	Joseph et al. <sup>9</sup>	<a href="https://www.ccpem.ac.uk/">https://www.ccpem.ac.uk/</a>
CCPEM	Wood et al. <sup>10</sup>	<a href="https://www.ccpem.ac.uk/">https://www.ccpem.ac.uk/</a>
pClamp	Molecular Devices	<a href="https://www.moleculardevices.com/">https://www.moleculardevices.com/</a>
CHARMM	Klauda et al. <sup>11</sup> Mackerell et al. <sup>12</sup>	<a href="https://academiccharmm.org/">https://academiccharmm.org/</a>
NAMD 2.13/2.14	Phillips et al. <sup>13</sup>	<a href="http://www.ks.uiuc.edu/Research/namd/">http://www.ks.uiuc.edu/Research/namd/</a>
MDFF	Trabuco et al. <sup>14</sup>	<a href="https://www.ks.uiuc.edu/Research/mdff/">https://www.ks.uiuc.edu/Research/mdff/</a>
MATLAB	MathWorks	<a href="https://www.mathworks.com/">https://www.mathworks.com/</a>
VMD	Humphrey et al. <sup>15</sup>	<a href="https://www.ks.uiuc.edu/Research/vmd/">https://www.ks.uiuc.edu/Research/vmd/</a>
<b>Other</b>		
200 mesh Cu R1.2/1.3 holey carbon grid	Quantifoil	Cat# N1-C14nCu20

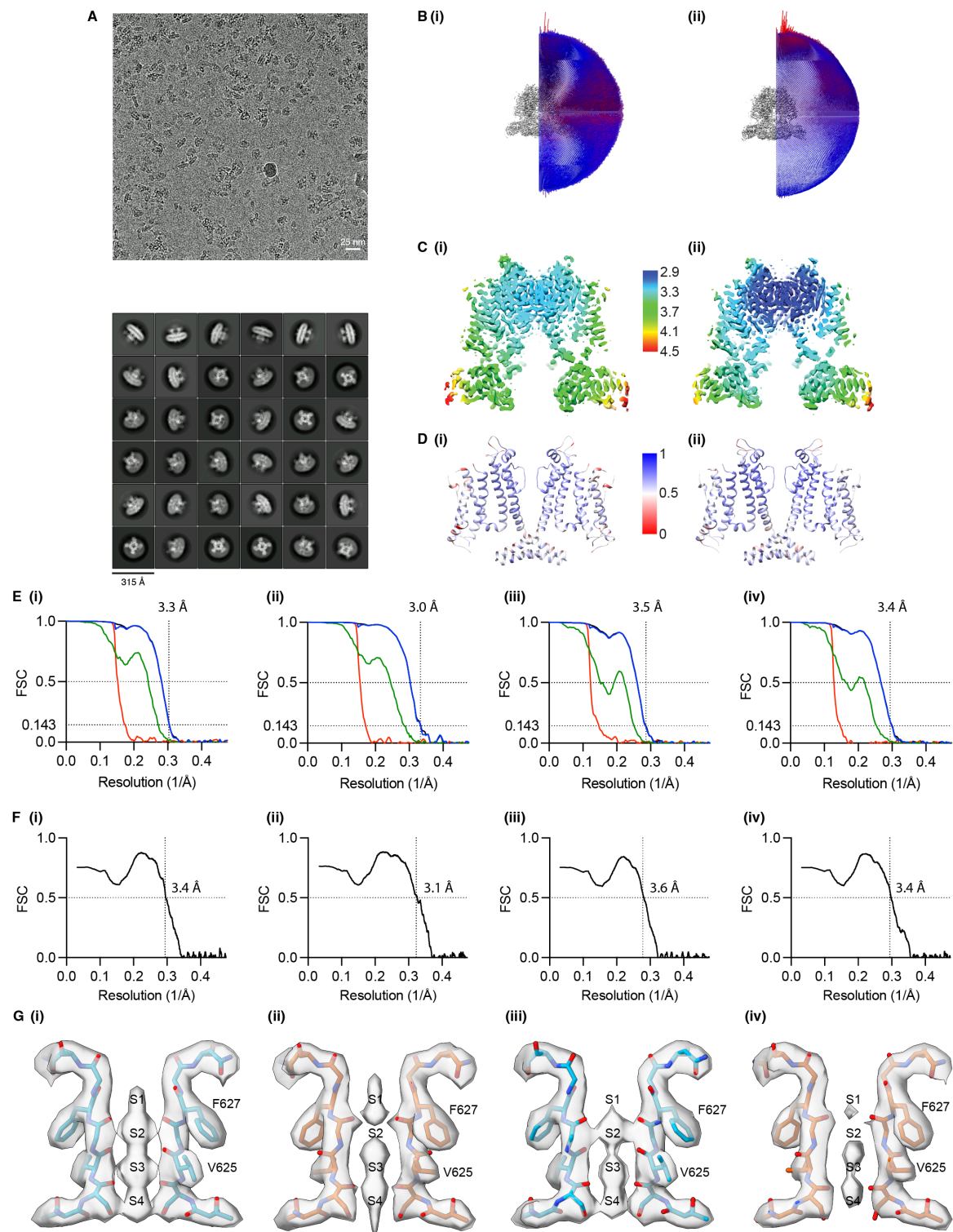
## Supplementary Fig S1



## Supplementary Fig S1: Cryo-EM data processing workflow

Flow chart of Cryo-EM data processing for high-K (cyan) and low-K (orange) datasets. Details can be found in Methods section.

## Supplementary Fig S2

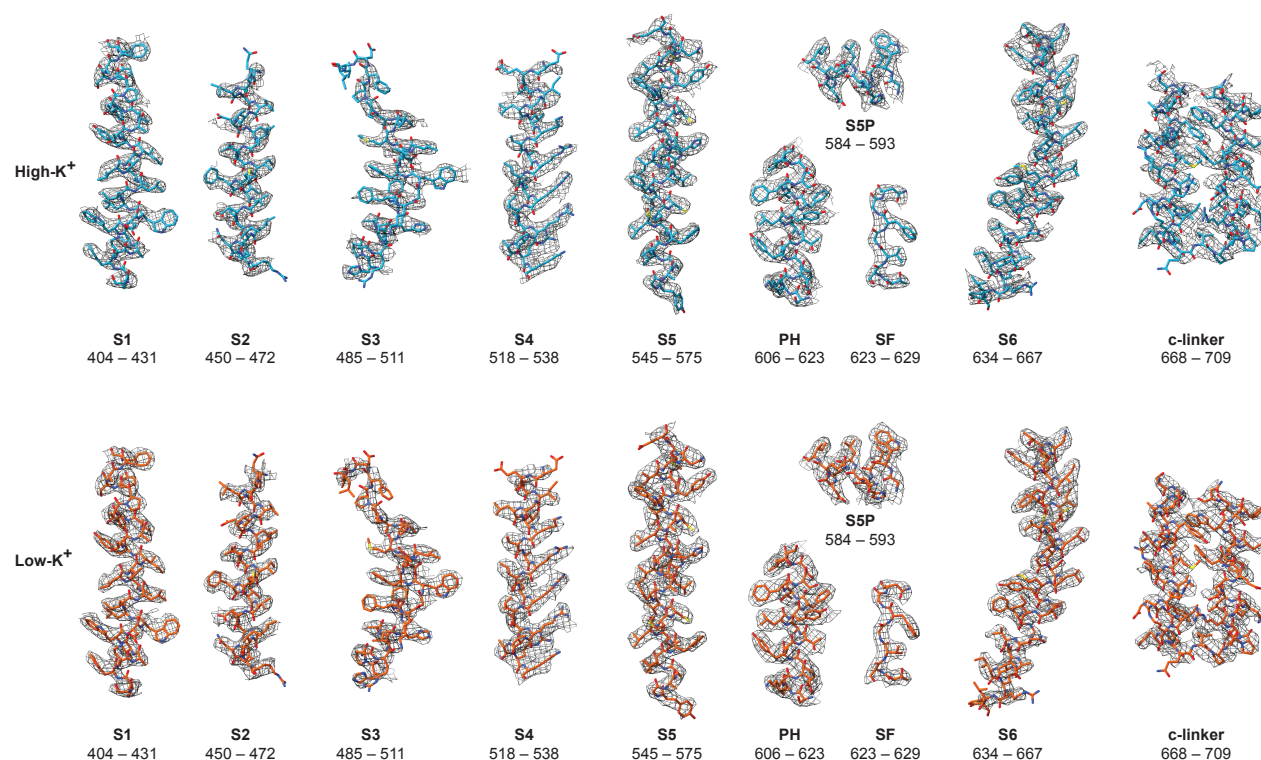


## Supplementary Figure S2: Cryo-EM validation

**A.** Representative electron micrograph and 2D class averages of hERG Ts for low-K dataset. **B.** Euler angle distribution of all particles used for final 3D reconstruction for (i) high-K and (ii) low-K dataset. **C.** Local resolution projected on a centre cross-section of the final 3D

reconstruction. **D.** Per-residue Q-score mapped onto corresponding models for (i) high-K and (ii) low-K structure). **E.** Gold-standard Fourier shell correlation (FSC) curve for the 3D reconstruction for (i) high-K with C4 symmetry, (ii) low-K with C4 symmetry, (iii) high-K with C1 symmetry, (iv) low-K with C1 symmetry. (Black: corrected map. Blue: masked maps. Red: phase randomized masked maps. Green: unmasked maps) **F.** Fourier shell correlation (FSC) curve between the map and model for (i) high-K with C4 symmetry, (ii) low-K with C4 symmetry, (iii) high-K with C1 symmetry, (iv) low-K with C1 symmetry. **G.** Cryo-EM map and PDB model showing two opposing subunits of the selectivity filter (623-629) for (i) high-K with C4 symmetry, (ii) low-K with C4 symmetry, (iii) high-K with C1 symmetry, (iv) low-K with C1 symmetry. Cryo-EM maps are shown at  $8\sigma$ . The main observable differences is for the densities lining the central axis in the vicinity of the  $K^+$  ion binding sites. These densities are more prominent in the C4 versus C1 maps. However, the differences between high K and low K maps are qualitatively similar; specifically in the low K maps there is (i) lower density at the top of the filter and (ii) reduced density at the S1-S2 boundary.

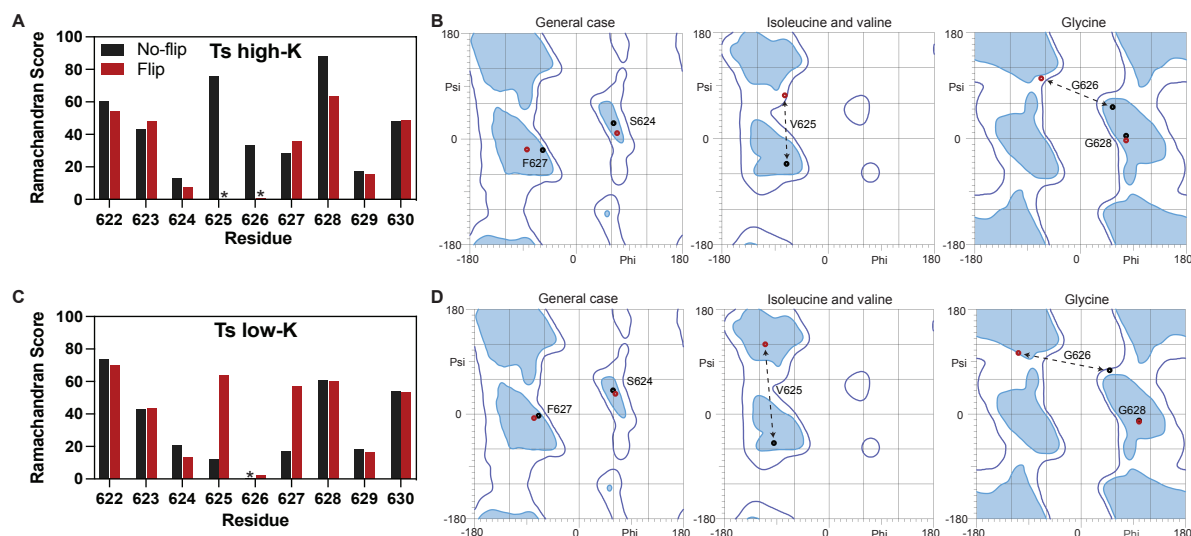
## Supplementary Fig S3



**Supplementary Fig S3: Cryo-EM density maps of selected regions of WT HERG in high-K (300 mM KCl) and low-K (3 mM KCl)**

Atomic models are shown as blue (high-K) and orange (low-K) sticks. Density maps are shown as grey wire mesh. Maps were sharpened using b-factor listed in Table S1.

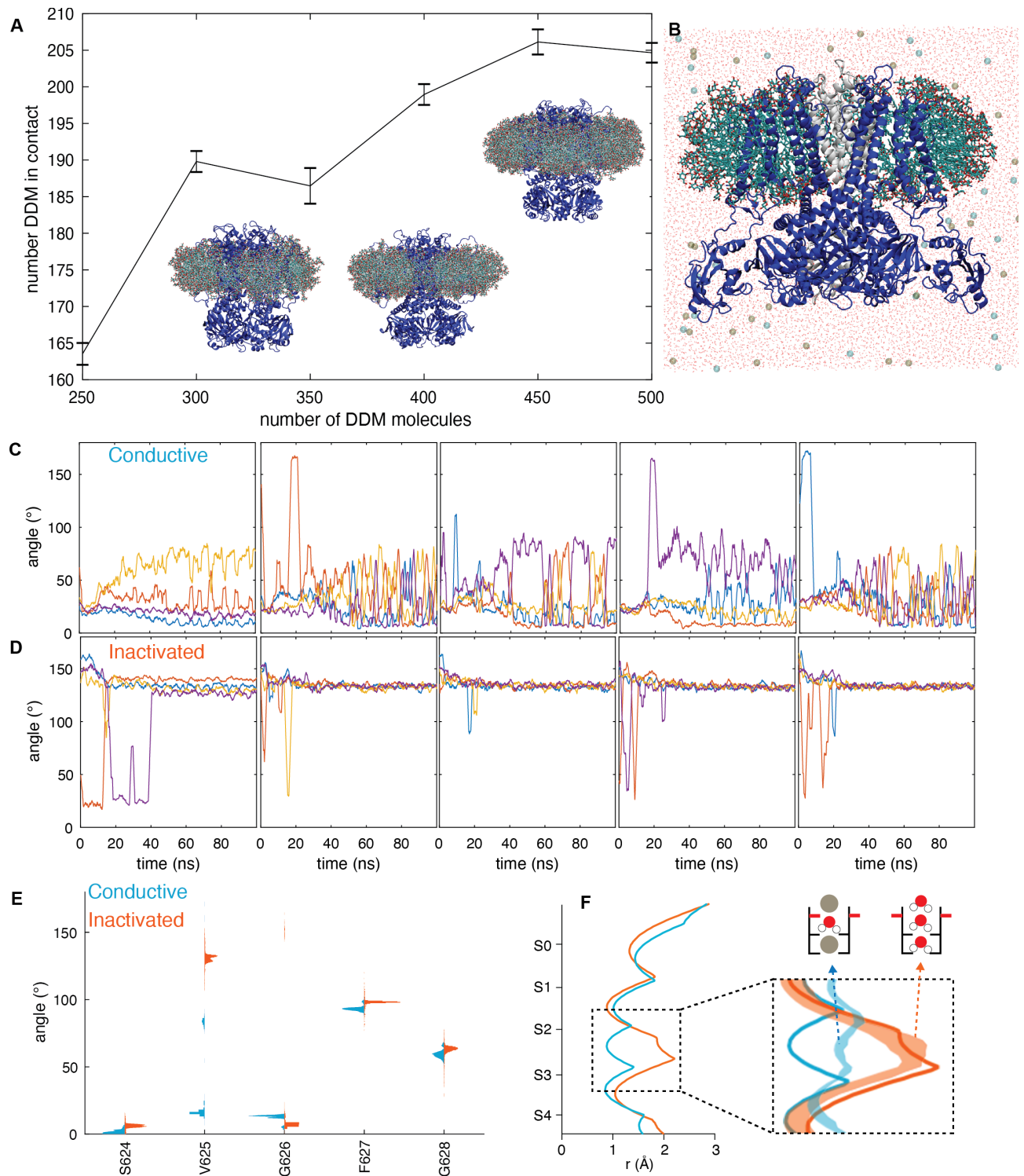
## Supplementary Fig S4



### Supplementary Fig S4: Comparison of Ramachandran statistics for flipped and non-flipped V625 carbonyl oxygen in high-K and low-K model

**A.** Summary of Ramachandran probability for flipped and non-flipped V625 carbonyl oxygen in high-K models. **B.** Ramachandran plots for residues 624–628 of flipped and non-flipped high-K model. **C.** Summary of Ramachandran probability for flipped and non-flipped V625 carbonyl oxygen in low-K models. **D.** Ramachandran plots for residues 624–628 of flipped and non-flipped low-K models. Residues with Ramachandran probability in allowed but not favored region are marked with asterisk (\*). Ramachandran plots for V625, G626, and G628 are plotted separately based on different Ramachandran probability distribution of these residues.

## Supplementary Fig S5



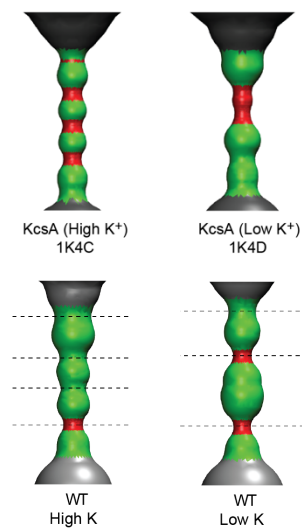
### Supplementary Fig S5 : MDFF fits to cryo-EM maps for high and low-K structures.

**A.** The optimal size of the micelle was determined by simulating HERG (PDB:5VA1) in 6 different sizes between 250 and 500 molecules of a simple pure detergent micelle (DDM). The number detergent molecules in contact with the protein is plateauing at 400-450 molecules showing that this is the

(Legend continued over page)

(shown in blue, with the TMD of the subunit at the front hidden and at the back in grey, for clarity) embedded in a micelle of 404 molecules consisting of detergent (DDM (300)), lipids (POPE (20), POPC (20), POPA (4)) and cholesterol derivative (cholesteryl hemisuccinate (60)) (shown as cyan (C), blue, (N), red (O) and olive (P) sticks) and surrounded by TIP3P water molecules<sup>56</sup> (shown as red sticks) and KCl (shown as olive and cyan spheres, respectively). **C-D.** Timeseries of the V625 carbonyl oxygen angle for the five independent MDFF simulations for high K channel with ions in S2/S4 (**C**) and low-K channel with an empty selectivity filter (**D**). For both systems, we see flipping and unflipping in the early part of the simulations. The high K channel converges to a mix of flipped and unflipped V625 carbonyl oxygens, whereas in the low-K channel all V625 are flipped at the end of the simulations. **E.** Distribution plots of the angle of the backbone carbonyl oxygens in the selectivity filter for the high (blue) and low (orange) K<sup>+</sup> structures based on 250 energy minimised structures extracted from MDFF simulations. **F.** Plot of the selectivity filter radius for the high K (blue) and low-K (orange) channel determined with HOLE<sup>7</sup>. Solid lines show the radius determined from the cryo-EM fit and shaded area the radius determined for the 250 energy minimised structures extracted from MDFF simulations. The decreased radius in the MDFF simulations compared to the cryo-EM fit at the V625 carbonyl oxygens (between S2 and S3) in the high K channel arise comes from the V625 carbonyl oxygens being in a mix of flipped and non-flipped states.

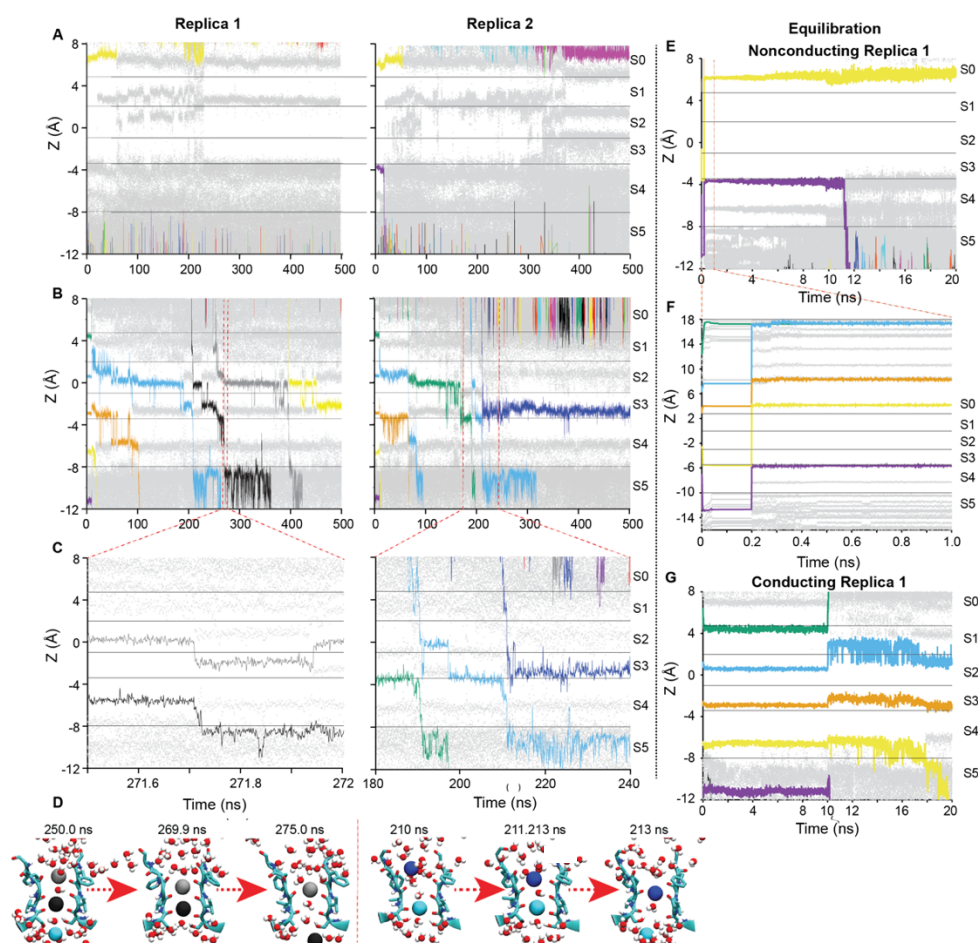
### Supplementary Fig S6



### Supplementary Fig S6: HOLE profiles for High-K and low-K HERG compared to High-K and low-K KcsA

Shape of ion conduction pathway calculated using HOLE. All models are aligned to the pore helix. The KcsA low-K profile is quite distinct to the HERG low-K structure, suggesting there may be different inactivation mechanism for the two channels.

## Supplementary Fig S7

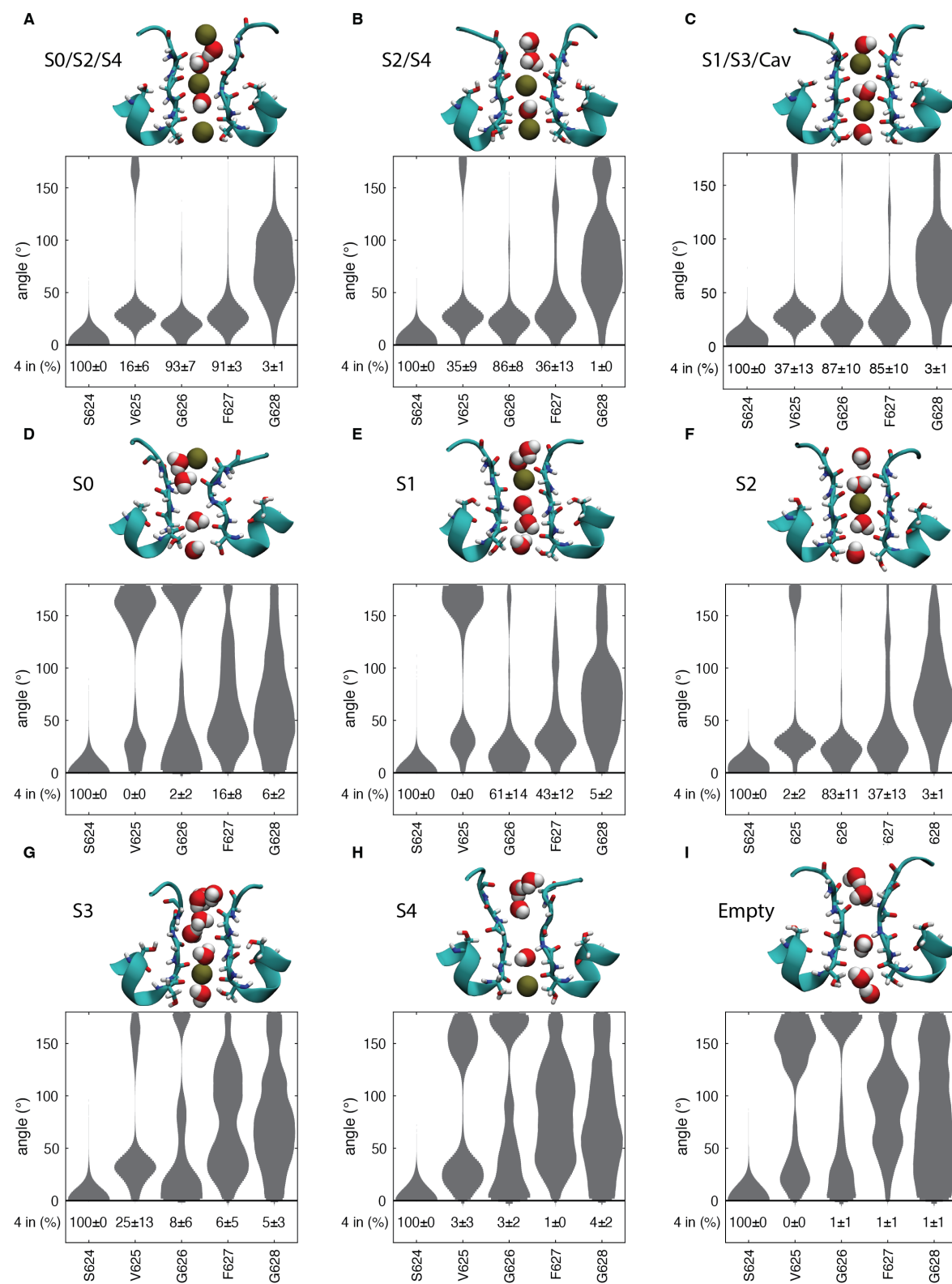


### Supplementary Fig S7: Ion conduction in HERG structures

Replica simulations for A. Low-K filter and B. High-K filter in the presence of a 500 mV gradient (inwards negative). Individual potassium ions are shown as colored lines, water molecules are shown as grey dots. In the low-K filter a loose constraint (see methods) was imposed to maintain the V625 carbonyl oxygens pointing outwards and in the high-K filter a loose constraint (see methods) was imposed to maintain the V625 carbonyl oxygens pointing inwards. A. There are no conduction events observed when V625 is carbonyls point outwards. B. With the V625 pointing inwards there are multiple ion-water-ion mediated (soft knock-on) conduction events. In the second simulation (right-hand panel), there are no conduction events after 225 ns, which correlates with an outward rotation ( $\sim 90^\circ$ ) of the F627 carbonyl oxygens and the presence of more water molecules in the upper filter. C. Expanded trace showing (i) the only example we observed of a hard knock on (ion-ion) event and (ii) an example of a soft knock-on (ion-water-ion) event. D. Structure snapshots taken at the times indicated to illustrate the ion conduction events highlighted in C. E. The 10 ns equilibration period of the nonconducting replica 1, plus another 10 ns of the production run (full production MD in panel A). Restraints on the ions inside the filter are decoupled slowly over the first 10 ns. F. First 1 ns of the equilibration phase from E., showing that, in the low-K filter, the ions leave the selectivity filter instantly. G. The 10 ns equilibration period of the conducting replica 1 where the selectivity filter ion restraints are slowly decoupled, plus another 10 ns of the production run. The 5 ions remain in the filter during the equilibration period, but the outermost ions leave immediately after the final restraints are released with

the filter then containing 2-3 ions. The redistribution of ions in the initial period were not included in our counts of ion conduction events.

## Supplementary Fig S8

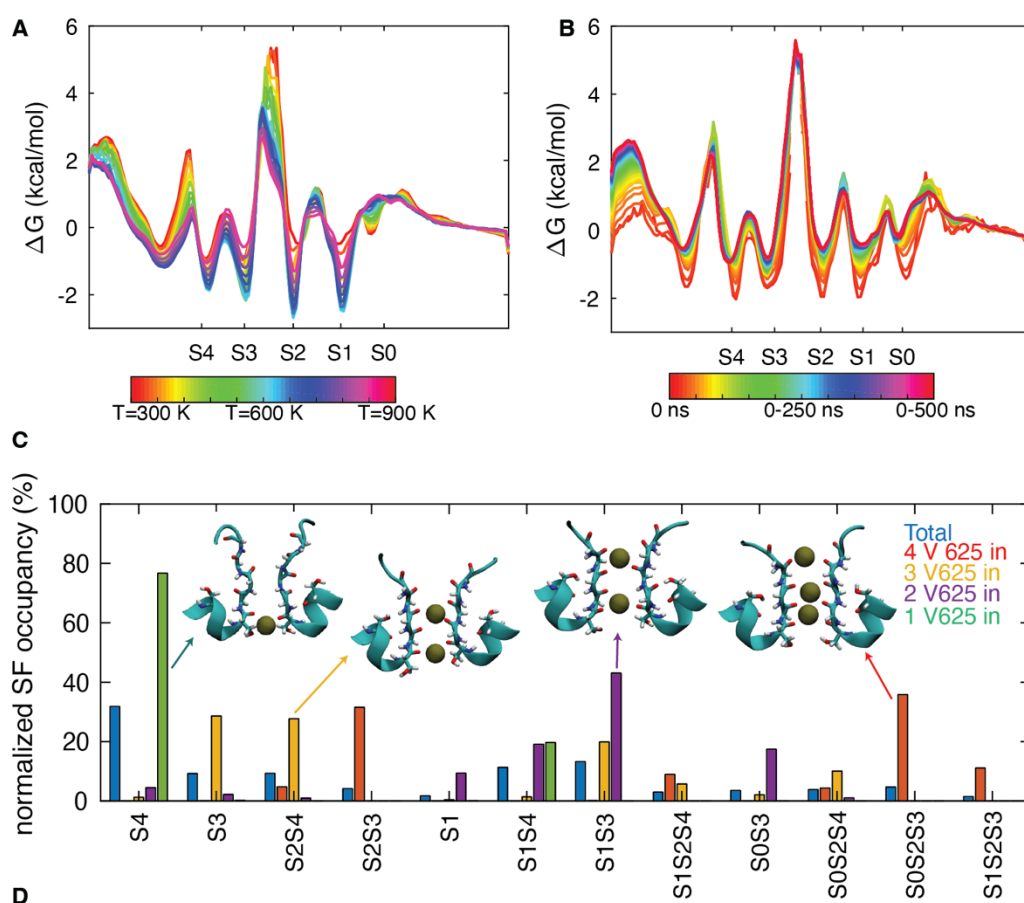


See overleaf for legend.

**Supplementary Fig S8: MD simulations to explore the effect of K<sup>+</sup> ions on selectivity filter conformation.**

Distribution plots of the angle of the backbone carbonyl oxygens in the selectivity filter (defined as the absolute value of the angle between the vector made up by C $\alpha$  and the carbonyl oxygen atom and C $\alpha$  and the center of mass of the selectivity filter) (top) and the frequency of four carbonyl oxygens pointing in (with an angle of < 70 degrees) (bottom) for ions held in **A.** S0/S2/S4, **B.** S1/S3/Cav, **C.** S2/S4, **D.** S0, **E.** S1, **F.** S2, **G.** S3, **H.** S4, and **I.** an empty selectivity filter. Insets in each panel show typical ion configurations. When K<sup>+</sup> ions were maintained in S0/S2/S4, S2/S4 or S1/S3/Cav (**A-C**), there were periods of time when V625 carbonyl oxygens were seen to flip to no longer be directed into the pore, with all four carbonyl oxygens pointing towards the channel axis only 16%, 35% and 37% of the time. However, when the filter was empty (**I**), there were never four V625 carbonyl oxygens pointing towards the channel axis. When an ion was placed in S0, S1 or S4 (**D,E,H**), the selectivity filter resembles that of the empty filter, with two or more carbonyl oxygens flipped 95%, 99% and 56% of the time, respectively, shown by a larger density of big angles in the probability like that of an empty selectivity filter (**I**). When an ion was placed in S2 or S3 (f and g), the selectivity filter resembles that of a filter with a multiple-ion configuration (carbonyl oxygens mostly directed inward with three or more carbonyl oxygens pointing in 94% and 80% of the time) (**A-C**). Even with an ion held in S2, we still observed that V625 can flip, with one or two flipping 91% and 6% of the time, respectively.

## Supplementary Fig S9



## Supplementary Fig S9: REST2 simulations

**A.** Free energy profile for all 16 replicas with temperatures varying from 300 K to 900 K for REST2 simulations<sup>32</sup>. Higher temperature replicas show shallower minima and lower barriers with well captured barriers between cavity-S4, S4-S3, S3-S2, and S2-S1. The free energy profile shows deepest binding in S2, S1 and S3. **B.** Convergence of the free energy profile for ions in the selectivity filter based on replica 0 (unscaled); converging to within ~1 kcal/mol within 70 ns. **C.** During REST2 simulations, we observed extensive fluctuations in the selectivity filter, with frequent flipping/unflipping of V625 carbonyl oxygens. PMF profiles for 0, 1, 2, 3, or 4 flipped V625 backbone carbonyls are shown in Figure 3D of the main manuscript. When all four V625 carbonyl oxygens were directed inward (13 % of the time; shown in red), there was on average 2.7 ions in the selectivity filter. Whilst canonical S2/S4 and S0/S2/S4 configurations were observed, most commonly ions were in S2/S3, S1S2S3, or S0/S2/S3 (depicted in the inset). When three V625 carbonyl oxygens were pointing in towards the channel axis (31% of the time; yellow), there was an average of 1.9 ions in the selectivity filter maintaining good binding in all sites with the most common configurations being S3 alone, S1S3, and S2S4 (depicted in inset). When two carbonyl oxygens were pointing inwards (16% of the time, almost exclusively in neighbouring subunits; purple) there was, on average, 2.0 ions in the selectivity filter, most commonly occupying S3 as well as S1 or S2 (purple). S3 and S4 have now merged into one site which is positioned around the Ser624 carbonyl oxygen plane. 39% of the time a single carbonyl oxygen was pointing in towards the channel axis (shown in green), with an average ion occupancy of 1.5. Now the ions almost exclusively bind to S4 and on the G626 carbonyl oxygen plane between S0 and S1, vacating the entire centre of the selectivity filter and prohibiting ion translocation. It was

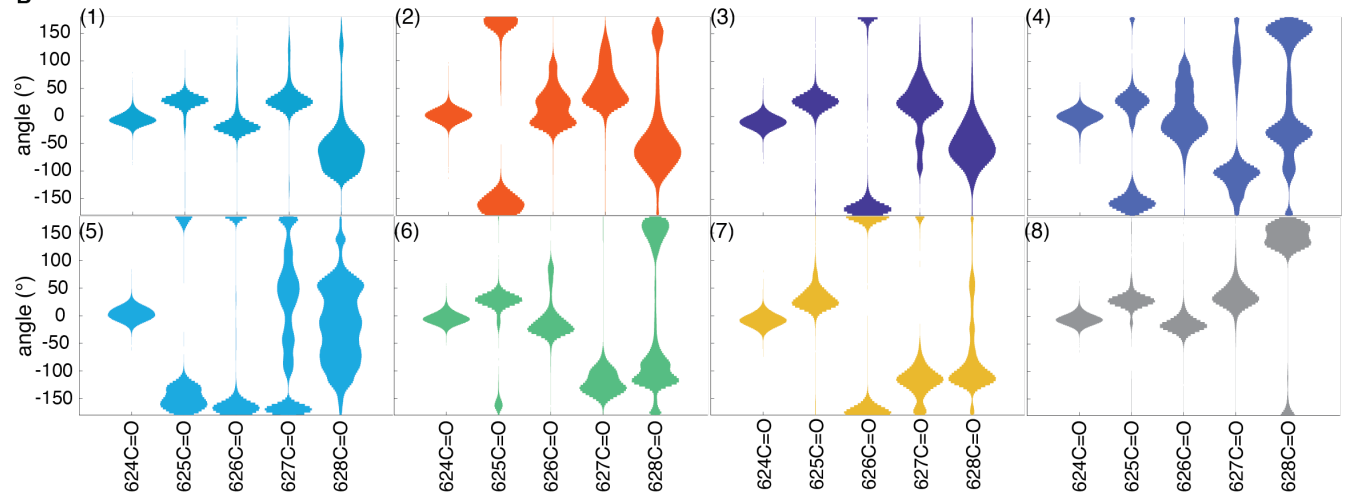
very unlikely (0.0052% of the time) that all V625 carbonyl oxygens were flipped outward (not shown).

## Supplementary Fig S10

A

	Cluster occupancy (%)							
Cluster	(1) Conductive- like	(2) Inactivated- like	(3) Flipped G626	(4) Flipped F627	(5) Flipped V625 and G626	(6) Flipped F627	(7) Flipped G626, F627 and G628	(8) Flipped G628
total	41	30	4.8	4.8	4.7	4.7	4.2	3.6
S0/S2/S4	73	22	0	0.61	0.025	0.062	0	3.8
S2/S4	64	17	0	1.1	0.055	8.9	0	8.2
S1/S3/Cav	71	17	2.4	2.2	0.33	1.4	0.14	5.7
S0	11	41	9.8	9.7	16	2.9	4	1.7
S1	25	53	4.4	8.3	3.8	3.7	0.73	1.2
S2	57	25	2.5	4.2	0.34	4.1	0.20	4.2
S3	45	21	6.1	2.9	0.054	10	6.3	4.0
S4	19	33	13	7.1	5.5	8.2	12	0.14
Empty	7.5	39	5.5	7.2	16	2.5	14	3

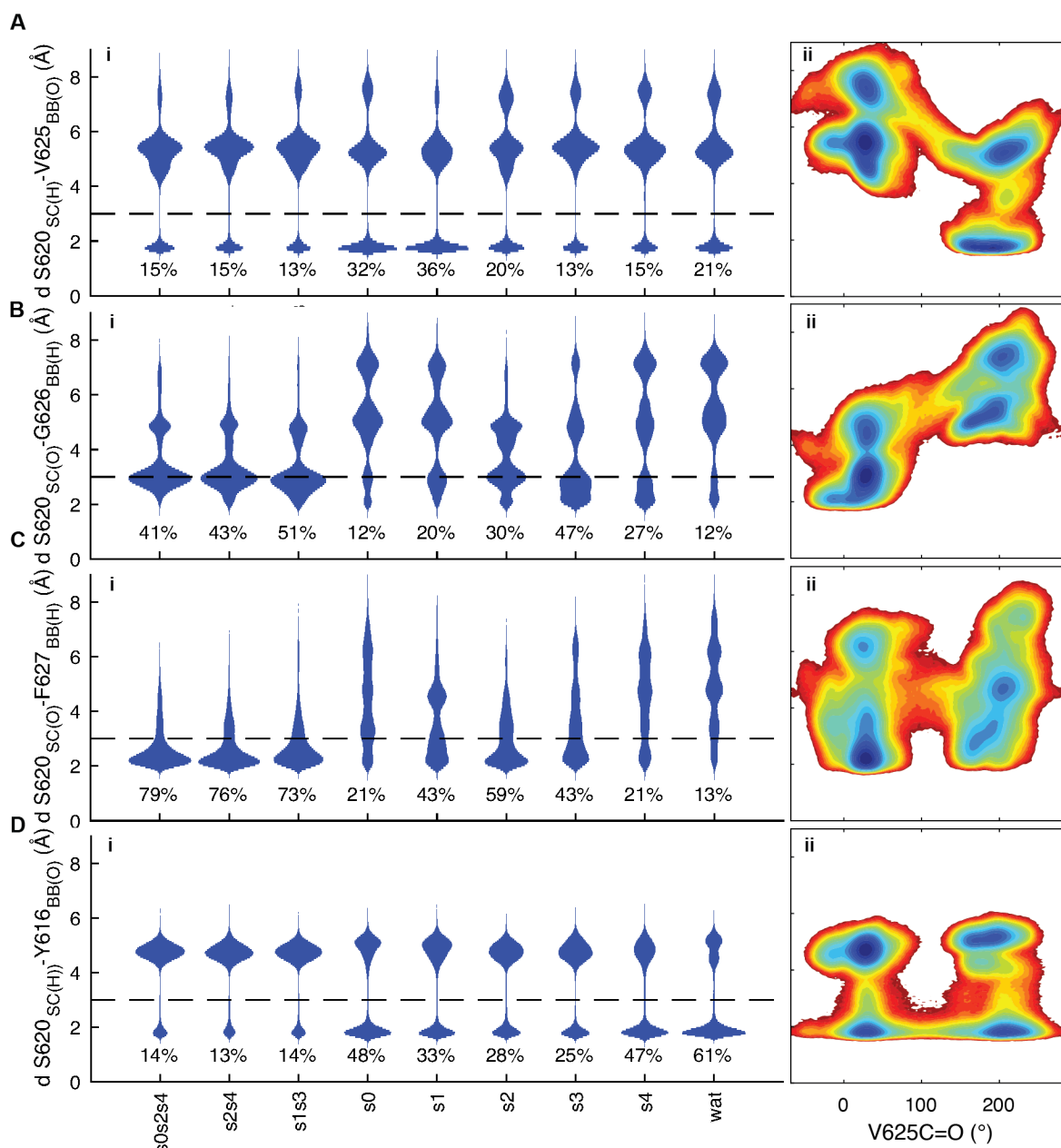
B



**Supplementary Fig S10: MD simulations with different K<sup>+</sup> ion conformations clustered according to backbone dihedral angles of each subunit of the selectivity filter.**

**A.** Table showing the occupancy (rows) for the 8 major clusters (labelled 1-8 in **A** and **B**) obtained from analysis of Selectivity Filter backbone atoms across all MD simulations (columns). The occupancy in each cluster across all simulations is shown on row 3 and for each ion-configuration simulation on rows 4-12. Cluster (1) shows a conductive-like state with the V625 carbonyl oxygen pointing towards the channel axis (41% total occupancy) and cluster (2) shows an inactivated-like state with the V625 carbonyl oxygen pointing out with a narrowing at G626 (30% total occupancy). Analysis of these two clusters are shown in Figure 3 in the main manuscript. The additional 6 clusters, which had various backbone residues flipped, had occupancies between 3% and 5%. When ions were placed in S0/S2/S4, S2/S4, S1/S3 or S2, the subunit maintained a conductive conformation most of the time (see columns 1,2 in panel A). This suggests that there must be multiple ions in the selectivity filter (including S2 or S3), or S2 must be occupied, for the selectivity filter to be conductive. **B.** Distribution plots of the angle of the backbone carbonyl oxygens in the selectivity filter for the 8 most observed clusters.

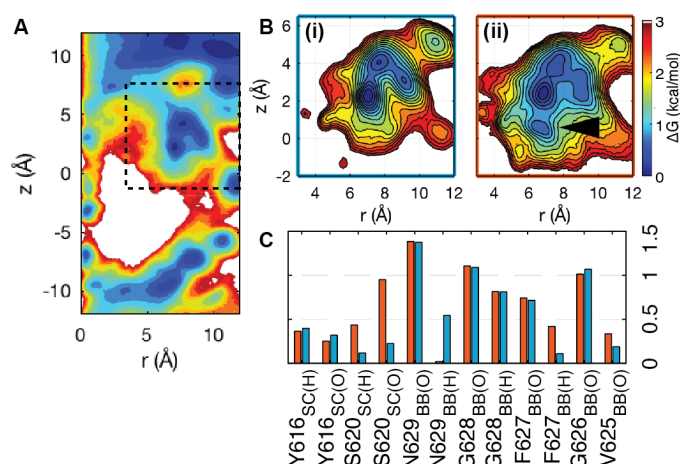
## Supplementary Fig S11



### Supplementary Fig S11: Interactions behind the selectivity filter for MD simulations with different K<sup>+</sup> ion conformations.

**A-D.** Distribution plots for the distance between the S620 sidechain hydroxyl and V625 C=O (**A**), G626 N-H (**B**), F627 NH (**C**) and Y616 C=O (**D**), as a function of ion occupancy of the filter (i) and 2-dimensional free energy plots as a function of rotation of the V625 carbonyl oxygen (ii). The 2D FEP obtained from the constrained ion MD, shown here, are very similar to what we observed with the REST2 simulations (see Figure 4C-F in main text).

## Supplementary Fig S12

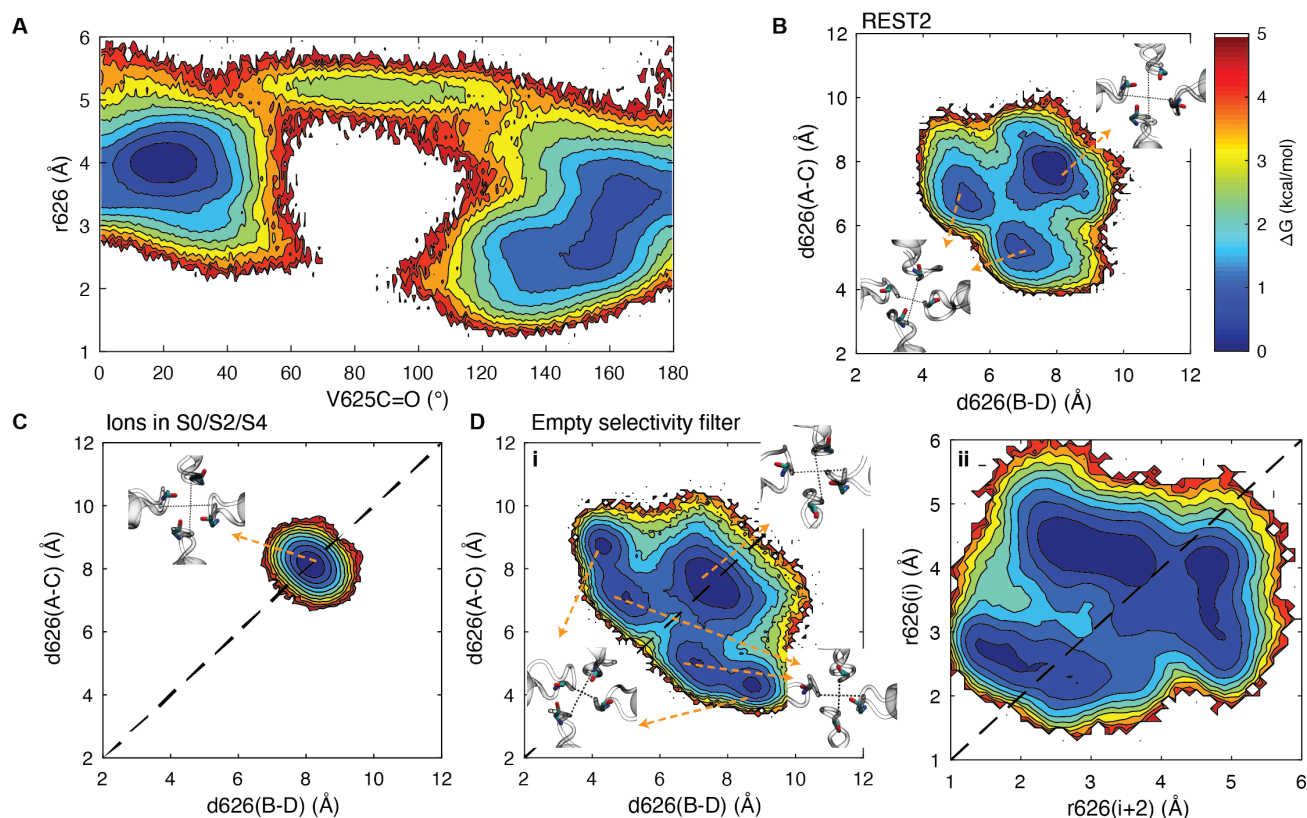


### Supplementary Fig S12: Changes in water distribution behind the selectivity filter in Cluster 1 (conducting) and Cluster 2 (non-conducting) states of HERG

**A.** Free energy distribution of number of water molecules behind the filter in all simulations.  $r = 0$  Å represents the central axis of the pore,  $z = 0$  Å represents the vertical component of the centre of mass of the selectivity filter. **B.** Free energy distribution of water molecules behind the filter in (i) conducting state (cluster 1, Supplementary Fig 9) and (ii) non-conducting state (cluster 2, Supplementary Fig 9). Arrowhead highlights an extra minimum in the non-conducting state. **C.** Mean number of interactions with water molecules behind the selectivity filter in conducting (blue) and non-conducting (orange) filters.

The additional minimum in the non-conducting state corresponds to a water molecule that predominantly interacts with the S620 side chain. This site is similar in location to the deepest water molecule in the inactivated KcsA structure although in KcsA that water binds to and stabilizes the pinched glycine amide<sup>17</sup>. There is also an increase in water bound to the F627 backbone amide when the V625 carbonyl oxygen is flipped, that compensates for F627 no longer interacting with S620 (C). It is notable that the total number of water molecules is not different between the flipped and non-flipped V625 carbonyl oxygen states of HERG (C), which is in marked contrast to KcsA, where the number of water molecules increases from one in the conductive state to three in the non-conductive state and this diffusion-limited transition plays a key role in establishing the slower inactivation kinetics of KcsA<sup>17</sup>.

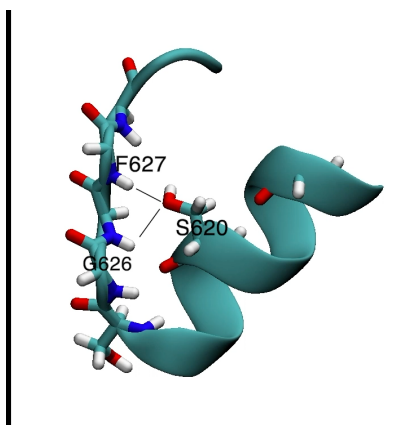
## Supplementary Fig S13



## Supplementary Fig S13: 2-dimensional free energy maps for V625 carbonyl oxygen flipping

**A.** 2-dimensional free energy maps highlighting the relationship between the flipping of the V625 carbonyl oxygen ( $>70^\circ$  away from the central axis) and the pinching of the G626 (represented as a mean radial position of G626 C $\alpha$  atoms,  $r626$ ). **B-D.** 2-dimensional free energy maps showing the pinching of G626 C $\alpha$  based on the distance between opposing subunits in: **B)** REST2 simulations **C)** MD simulations with ions constrained in S0/S2/S4; **Di)** MD simulations for an empty selectivity filter. Insets show representative cross section images at the level of G626 C $\alpha$ . **Dii.** 2-dimensional free energy map showing the relationship between the radial positions of G626 C $\alpha$  in two opposing subunits during the pinching of G626. Although **Di** suggests an asymmetric collapse with 2-fold symmetry, it is apparent from **dii** that this arises predominantly due to movements only in one of the two subunits, which contrasts with the C2 symmetrical inactivated state suggested by Li and colleagues<sup>24</sup>.

## Supplementary Movie 1



### **Supplementary Movie 1. Interactions between S620 and the selectivity filter during the transition between conducting and non-conducting structures**

Movie showing how the S620 sidechain can interact with the backbone of G626 and F627 (H) or the backbone of Y616 (O) in the conductive state (Figure 4 D-G (i), main text). When the sidechain of r620 interacts with the backbone of Y616 (O) ((Figure 4 D-G (ii),(iii) main text), the V625 carbonyl oxygen can flip outward. The sidechain of S620 can then interact with the backbone of V625 (O) (Figure 4 C-F (iv), main text) in the inactivated state.

## Supplementary References

- 1 Ng, C. A. et al. Heterozygous KCNH2 variant phenotyping using Flp-In HEK293 and high-throughput automated patch clamp electrophysiology. *Biol Methods Protoc* 6, bpab003 (2021). <https://doi.org/10.1093/biomethods/bpab003>
- 2 Zivanov, J. et al. New tools for automated high-resolution cryo-EM structure determination in RELION-3. *Elife* 7 (2018).
- 3 Pettersen, E. F. et al. UCSF ChimeraX: Structure visualization for researchers, educators, and developers. *Protein Sci* 30, 70-82 (2021). <https://doi.org/10.1002/pro.3943>
- 4 Croll, T. I. ISOLDE: a physically realistic environment for model building into low-resolution electron-density maps. *Acta Crystallogr D Struct Biol* 74, 519-530 (2018).
- 5 Rohou, A. & Grigorieff, N. CTFFIND4: Fast and accurate defocus estimation from electron micrographs. *J Struct Biol* 192, 216-221 (2015).
- 6 Liebschner, D. et al. Macromolecular structure determination using X-rays, neutrons and electrons: recent developments in Phenix. *Acta Crystallogr D Struct Biol* 75, 861-877 (2019).
- 7 Smart, O. S., Neduelil, J. G., Wang, X., Wallace, B. A. & Sansom, M. S. HOLE: a program for the analysis of the pore dimensions of ion channel structural models. *J Mol Graph* 14, 354-360, 376 (1996).
- 8 Chen, V. B. et al. MolProbity: all-atom structure validation for macromolecular crystallography. *Acta Crystallogr D Biol Crystallogr* 66, 12-21 (2010). <https://doi.org/10.1107/S0907444909042073>
- 9 Joseph, A. P. et al. Comparing Cryo-EM Reconstructions and Validating Atomic Model Fit Using Difference Maps. *J Chem Inf Model* 60, 2552-2560 (2020). <https://doi.org/10.1021/acs.jcim.9b01103>
- 10 Wood, C. et al. Collaborative computational project for electron cryo-microscopy. *Acta Crystallogr D Biol Crystallogr* 71, 123-126 (2015). <https://doi.org/10.1107/S1399004714018070>
- 11 Klauda, J. B. et al. Update of the CHARMM all-atom additive force field for lipids: validation on six lipid types. *J Phys Chem B* 114, 7830-7843 (2010).
- 12 Mackerell, A. D., Jr., Feig, M. & Brooks, C. L., 3rd. Extending the treatment of backbone energetics in protein force fields: limitations of gas-phase quantum mechanics in reproducing protein conformational distributions in molecular dynamics simulations. *J Comput Chem* 25, 1400-1415 (2004).
- 13 Phillips, J. C. et al. Scalable molecular dynamics with NAMD. *J Comput Chem* 26, 1781-1802 (2005).
- 14 Trabuco, L. G., Villa, E., Mitra, K., Frank, J. & Schulten, K. Flexible fitting of atomic structures into electron microscopy maps using molecular dynamics. *Structure* 16, 673-683 (2008).
- 15 Humphrey, W., Dalke, A. & Schulten, K. VMD: visual molecular dynamics. *J Mol Graph* 14, 33-38, 27-38 (1996). [https://doi.org/10.1016/0263-7855\(96\)00018-5](https://doi.org/10.1016/0263-7855(96)00018-5)